Journal of Biomedical Optics

BiomedicalOptics.SPIEDigitalLibrary.org

Monte Carlo analysis of the enhanced transcranial penetration using distributed near-infrared emitter array

Lan Yue
Mark S. Humayun

SPIE.

Journal of Biomedical Optics 20(8), 088001 (August 2015)

Monte Carlo analysis of the enhanced transcranial penetration using distributed near-infrared emitter array

Lan Yue* **and Mark S. Humayun***
University of Southern California, Institute for Biomedical Therapeutics, USC Eye Institute, 1441 Eastlake Avenue, NTT Room 4463, Los Angeles, California 90033, United States

Abstract. Transcranial near-infrared (NIR) treatment of neurological diseases has gained recent momentum. However, the low NIR dose available to the brain, which shows severe scattering and absorption of the photons by human tissues, largely limits its effectiveness in clinical use. Hereby, we propose to take advantage of the strong scattering effect of the cranial tissues by applying an evenly distributed multiunit emitter array on the scalp to enhance the cerebral photon density while maintaining each single emitter operating under the safe thermal limit. By employing the Monte Carlo method, we simulated the transcranial propagation of the array emitted light and demonstrated markedly enhanced intracranial photon flux as well as improved uniformity of the photon distribution. These enhancements are correlated with the source location, density, and wavelength of light. To the best of our knowledge, we present the first systematic analysis of the intracranial light field established by the scalp-applied multisource array and reveal a strategy for the optimization of the therapeutic effects of the NIR radiation. [DOI: 10.1117/1.JBO.20.8.088001]

Keywords: Monte Carlo; near infrared; emitter array; transcranial propagation; scatter; tissues.

Paper 150324PR received May 19, 2015; accepted for publication Jul. 8, 2015; published online Aug. 7, 2015.

1 Introduction

Noninvasive optical approaches for the treatment of neurological disorders have received increasing attention in recent years. A number of *in vitro* and *in vivo* studies have demonstrated the therapeutic potentials of low-level near-infrared (NIR) light in ameliorating brain damages caused by ischemia, traumatic injury, and neurodegeneration.[1] Notably, transcranial radiation of an 808-nm laser NIR light was found to produce beneficial outcomes in poststroke rats[2] and embolized rabbits,[3] though the clinical effectiveness in human subjects is still under debate.[4–7] The use of NIR in the treatment of mild traumatic brain injury (mTBI) has also been reported, both in animal models and in humans.[8–13] The transcranial radiation with 870-nm NIR LED cluster heads was shown to improve cognitive function, sleep, and post-traumatic stress disorder symptoms in chronic mTBI patients.[13] NIR therapies for depression, Alzheimer's disease, and Parkinson's disease are currently under investigation by various groups in mouse models and in clinical studies.[14–16] Though the molecular mechanisms are not yet fully understood, popular hypotheses link the physiological modulation of the NIR radiation to neuron protection and cellular metabolism arising from improved mitochondrial function. Cytochrome C oxidase, the key mitochondrial component involved, has a broad absorption range that peaks around 830 nm.[17] Upregulation of the neuroprotective gene products and increased neurogenesis, for example, in lateral ventricles and the hippocampus, are also associated with the action of NIR radiation.[1,8,18–20]

Despite the exciting findings by these groundbreaking works, limited penetration remains a major barrier in boosting the effectiveness of the NIR treatment. Extracranially applied NIR light undergoes exponential decay in the magnitude of the photon flux as it travels through the highly scattering overlying tissues, including the scalp and skull, of an adult human head. Only a very small fraction of the light arrives at the cortex surface, largely limiting the NIR dose received by the brain. A similar problem occurs in NIR spectroscopy and other noninvasive optical brain imaging modalities that typically reflect, for instance, oxygenation and hemodynamics of the cortex. Therapeutically or diagnostically used low-level NIR sources frequently operate at an output power ranging from tens to hundreds of milliwatts with wavelengths of 600 to 1000 nm. Our previous studies showed that a high-power (495 mW) 850 nm LED merely produced a local photon flux of 20 to 60 $\mu W/cm^2$ along the propagation axial after the light passed through tissue blocks consisting of scalp, skull, dura, and 1 to 4 cm thick brain.[21] Substitution with an extra high-power LED emission is less favorable because not only does it offer rather limited photon flux increment due to its incoherent and divergent nature, but also it may introduce increased thermal risks to the radiated tissues. LEDs in direct contact with the skin or scalp are known to produce thermal effects on tissues in two forms: radiated and conducted heat. Despite the low-cerebral absorption of the radiated energy,[22] the conducted heat, caused by temperature rise in the semiconductor junction of the NIR emitters, is not negligible. An elevation as high as 10°C in skin temperature was reported using an 850-nm LED with a peak output of 37.5 mW/cm^2.[23]

Here, we propose to use an LED array with multiple emitters evenly distributed on the scalp for improved transcranial penetration, assuming that superposition of the laterally scattered

*Address all correspondence to: Lan Yue, E-mail: lyue@usc.edu; Mark S. Humayun, E-mail: humayun@med.usc.edu

1083-3668/2015/$25.00 © 2015 SPIE

photons emitted from multiple sources will result in increased intracranial photon density. Our earlier measurement from cadaveric human tissues finds very little variation in the NIR penetration effectiveness through different cranial sites, for instance, in the occipital, parietal, temporal, and frontal regions.[21] This result supports the hypothesis that similarly powered emitters, when evenly spaced, are capable of producing photon distribution of improved uniformity in the brain. With each individual emitter in the array operating under the safe limit, this approach could potentially achieve enhanced photon flux while minimizing the conducted heat to the scalp. In this study, by employing the Monte Carlo method to simulate the transcranial propagation of the array emitted light, we draw a comprehensive picture of the cross-enhancement of the photon flux by multiple sources. Furthermore, a conceptual design of the proposed radiation system is explored. To the best of our knowledge, this study presents the first systematic analysis of the intracranial light field established by the scalp-applied multisource array.

2 Methods

2.1 *Human Head Model*

The widely-used Colin27 brain template, consisting of $1 \times 1 \times 1$ mm^3 voxels of 256 gray levels, is adopted as the anatomical human head model in our simulation.[24] The volumetric template was filtered for reduced intensity nonuniformity and then segmented into five tissue types [scalp, skull, cerebrospinal fluid (CSF), gray matter, and white matter] using SPM12, a statistical parametric mapping-based brain image analysis software (Fig. 1). All voxels were labeled by tissue types containing the corresponding light properties: absorption coefficient, transport scattering coefficient, and approximate refractive index for light within the simulated wavelength range. This model is described in a Cartesian coordinate system, with the center of the head at (111.5, 91, 30).

2.2 *Light Source-Array on the Head Model*

The head model was first translated in the coordinate system such that it is centered at the origin. The brain was treated as hemispherical in shape with its equator tilted from the x–y plane at an angle of 0.09 rad. In order to evenly distribute light sources on the scalp, it is mathematically convenient to have the brain's equator sit on the x–y plane and henceforth consider the spatial arrangement of the light sources in spherical coordinates. The coordinate frame was, therefore, rotated 0.09 rad counterclockwise about the y-axis. The rotated z-axis now points toward the north pole of the brain hemisphere. Point sources representing the LED emitters in an array are distributed on the scalp such that the projection of all point sources on the unit sphere shares similar spacing, as quantified by the solid angle of a curved quadrilateral formed between any four neighboring points. The solid angle is defined as $\cos\theta \cdot \Delta\theta \cdot \Delta\phi$, where θ and ϕ are conventionally defined as the elevation and the azimuthal angle, respectively. Thus $\Delta\theta$ and $\cos\theta\Delta\phi$ represent the latitudinal and the longitudinal separation between given neighboring sources. An exception was made for the north pole source, which, as the single point at $\theta = (\pi/2)$, has $\Delta\phi$ undefined

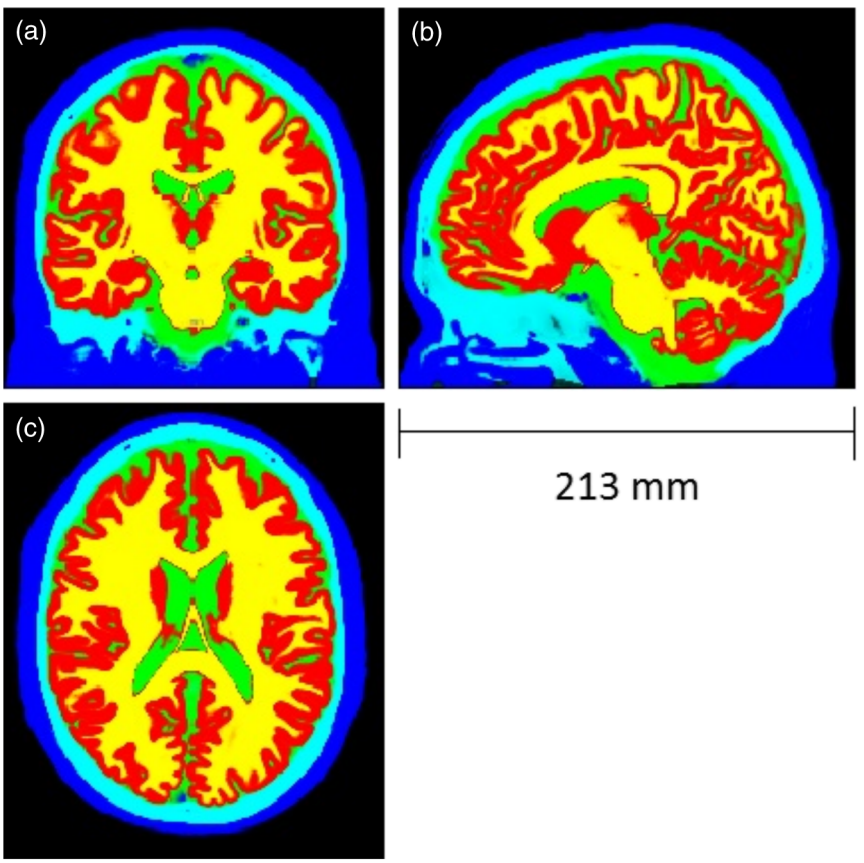

Fig. 1 Sections of the segmented head model [(a): frontal view at $x = 100$ mm; (b): sagittal view at $y = 110$ mm; (c) top view at $z = 91$ mm]. The blue, cyan, green, red, yellow color labeled segments represent the scalp, skull, CSF, gray matter, and white matter, respectively.

Table 1 Spatial arrangement of 277 light sources on the head model and the corresponding solid angles.

Layer	Elevation (θ)	Increment of Azimuth in each layer ($\Delta\phi$)	Solid angle ($\Delta\Omega$)	Theoretical number of light sources per elevation layer	Rounded to the nearest multiplication of 4	Actual value of $\Delta\phi$	Actual value of $\Delta\Omega$
1	0	0.157	0.025	40.00	40	0.157	0.025
2	0.157	0.159	0.025	39.51	40	0.157	0.024
3	0.314	0.165	0.025	38.04	36	0.175	0.026
4	0.471	0.176	0.025	35.64	36	0.175	0.024
5	0.628	0.194	0.025	32.36	32	0.196	0.025
6	0.785	0.222	0.025	28.28	28	0.224	0.025
7	0.942	0.267	0.025	23.51	24	0.262	0.024
8	1.100	0.346	0.025	18.16	20	0.314	0.022
9	1.257	0.508	0.025	12.36	12	0.524	0.025
10	1.414	1.004	0.025	6.26	8	0.785	0.019
11	1.571				1		
Weighted average of actual $\Delta\Omega$						2.451×10^{-2}	
Standard deviation (SD) of actual $\Delta\Omega$						1.233×10^{-3}	
SD over average						5.03%	

and is, therefore, excluded from the distribution calculation. At the maximum source density in our simulation, a total of 277 sources were arranged in a 0.05 radian elevation grid (Table 1), with an average solid angle of 0.0245 ± 0.0012 [mean $\pm$ standard deviation (SD)]. Reduced source densities, corresponding to higher values of solid angles, were studied as well.

2.3 *Monte Carlo Simulation*

Transcranial light propagation was simulated using a Monte Carlo approach, implemented under MATLAB® environment MXCLab[25] that describes photon migration in a complex three-dimensional (3-D) medium. Unless otherwise stated, due to its wide use and excellent tissue responsiveness, we employed 850-nm NIR in our simulation and the optical properties of different tissue types at this particular wavelength were obtained from previous studies[26–28] (Table 2). The propagation direction of each single source is defined as the initial direction of photon injection along the spherical normal toward the center of the head model. A total of 10^9 hotons were launched from each light source and each individual photon was traced as it propagated through the medium. All photons were initially assigned with a unit weight. As a photon propagates from one scattering event to the next, the weight is reduced by a factor of $e^{-\mu_a L}$ due to absorption, where μ_a is the absorption coefficient and L is the length traveled by the photon. The change in weight is then deposited into the voxel that contains the scattering event. The scattering angle is obtained using the probability distribution given by the Henyey–Greenstein phase function of a random variable.[29] The photon is subsequently migrated in this updated direction by a new scattering length that is determined with an exponential function. These steps were repeated until the photon exited the medium or has traveled an exceedingly long time in the medium. As the human head model contains spatially varying optical parameters, this algorithm checks every voxel spacing for new parameters to ensure the correct calculation of the weight decrease, the scattering angle, and the length. The weight of all photons dropped within each voxel was added to yield the photon flux produced by each individual light source. Furthermore, the photon flux contributed by all simulated sources was superimposed to generate a comprehensive light field map produced by multiple sources. The diffusion coefficient employed in this study is the reduced diffusion coefficient (μ_s') that already takes account of the anisotropic scattering in the isotropic assumption. Unless otherwise stated, a Gaussian-beam was opted for each source to best mimic the light emission profile of an actual LED source.

Table 2 Optical properties of the tissue types at the wavelengths of 850 and 690 nm.

	μ_a (mm^{-1})		μ_s' (mm^{-1})	
Tissue type	850 nm	690 nm	850 nm	690 nm
Scalp	0.012	0.021	1.8	2.37
Skull	0.025	0.026	1.6	2.35
Modified CSF	0.003	0.0004	0.01	0.01
Gray matter	0.036	0.036	0.9	1.4
White matter	0.014	0.014	1.1	1.5

2.4 *Finite Element Analysis*

The diffusion approximation of the radio transfer equation[30–32] has also been widely used to describe the light propagation in highly-scattering biological tissues, under the assumption that the absorption coefficient is considerably smaller than the scattering coefficient and that the light propagation is isotropic. The diffusion equation is given by

$$-\nabla \cdot \kappa(r)\nabla\Phi(r) + \mu_a(r)\Phi(r) = q_0(r), \quad (1)$$

where Φ is the photon fluence, κ is the diffusion coefficient $[3(\mu_a + \mu_s')]^{-1}$, and q_0 is the isotropic source distribution at r. The photon diffusion at the head-source interfaces were constrained by the surface Robin boundary condition, whereas at the tissue-tissue interfaces, fluence continuity in the normal direction was assumed. A finite element analysis (FEA) model was constructed using COMSOL Multiphysics to estimate the photon distribution in a multilayered 3-D domain that represents an adult human head. The geometry of the model, imported from the COMSOL Multiphysics library, was minimally modified from the original geometry provided by IEEE, IEC, and CENELEC. The light sources, represented by 0.4-cm diameter illumination spots, were positioned on the scalp at an average interunit distance of 2 cm. A detailed description of our approach can be found in Ref. 21.

3 Results

3.1 *Influence on Near-Infrared Penetration by the Source Location*

In order to compare the penetration effectiveness of the NIR light that enters different cerebral lobes, the axial attenuations of the photon flux emitted by five identical sources were examined: four randomly placed in the frontal, occipital, temporal, and parietal regions, respectively, and an additional one located at the north pole, as shown in Fig. 2(a). Light emitted by these sources exhibited similar attenuation profiles along the propagation direction, with only the occipital and temporal sources showing slightly more resistance to the NIR penetration, particularly in deep brain [Fig. 2(b)]. This result resembles, yet slightly deviates from our earlier measurements on a cadaveric human head that showed even greater similarity in the NIR penetration ability through various lobes. However, considering a typically greater skull thickness in the occipital region and the nontrivial intersample variations in the size of the excised brain we measured, the small difference between the measured and the simulated results is not surprising. Nonetheless, the comparable NIR penetration effectiveness in different cerebral lobes strongly suggests that output tuning/compensation for each individual source may not be required to establish a quasispherically symmetric light field and thus is not included in our subsequent simulations.

3.2 *Photon Flux Map Produced by Multiple Sources*

Figure 3 shows the results obtained from the simulation with 277 sources evenly distributed on the scalp (panel a), attaining an average solid angle of 0.024 ± 0.002 (mean $\pm$ SD). This high-source density produced a radially quasisymmetrical light field that exhibited little variation at similar penetration depths across the entire head model, as illustrated by the rainbow-shaped color maps of the intracranial photon flux, in both the frontal (panels b and c) and the sagittal views (panels d and e). The central dip of the penetration profile in the frontal slice shown in panel c arises from the interhemispherical fissure of the brain. Under the influence of such densely packed sources, the axial evolvement of the photon distribution was examined at the five previously picked sources, one located at the north pole and the rest in the frontal, the occipital, the temporal, and the parietal regions, respectively. The one-dimensional representation of the results (panel f) reveals comparable attenuation patterns for all five sources, despite slightly stronger decay in the occipital and the temporal regions, as the light passed further down into the brain.

In comparison with the single source results, this multisource simulation yielded a photon flux enhancement that is progressively substantialized along the propagation direction (Fig. 4). Fitted by a single exponential function ($\tau = 34.7 \pm 2.9$ mm^{-1}, $R^2 = 0.995$), the ratio of the photon flux (i.e., the gain) produced by a multi (circles) versus a single (squares) source along the propagation direction of the north pole source demonstrates the dependence of the enhancement effect on the penetration depth (black diamonds). Robust enhancement initiated around 20-mm deep, approximately at the upper-mid cortex level. Beyond this depth, the gain increased to about 5× at 40 mm, doubling to 10× at 60 mm, and finally reached >40× at 100 mm depth. This

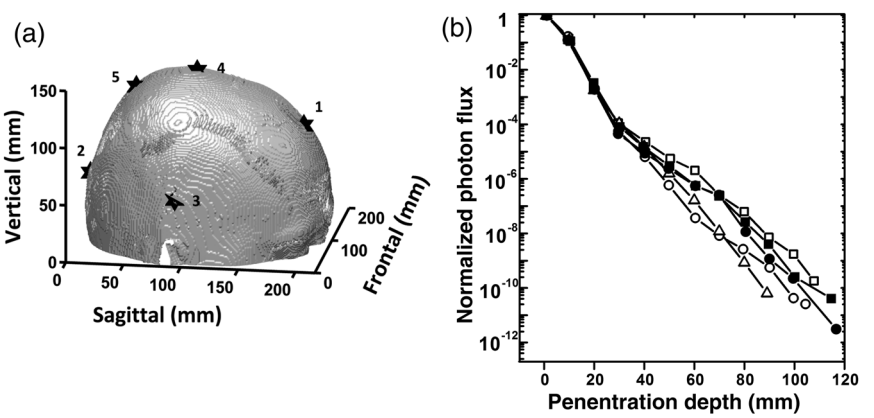

Fig. 2 The single source penetration profiles: (a) locations of the single sources on the scalp: frontal (1), occipital (2), temporal (3), parietal (4), and north pole (5) source in the source coordinates; (b) penetration profiles of the frontal (open square), occipital (open circle), temporal (open triangle), parietal (filled circle), and north pole (filled square) source along the corresponding propagation directions.

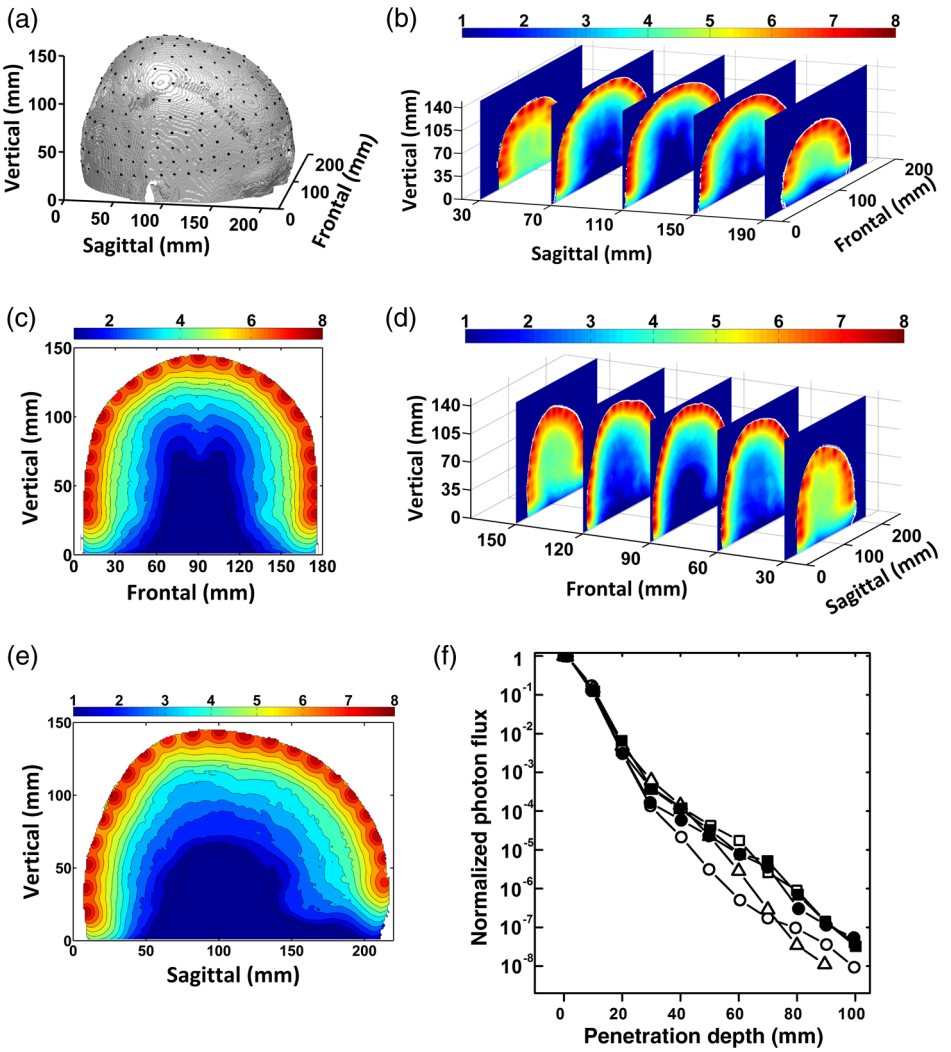

Fig. 3 Light field produced by 277 sources (850 nm, Gaussian beam). Color bars: orders of magnitude of photon flux: (a) spatial distribution of the 277 point sources on the scalp; (b) frontal slice views of the three-dimensional (3-D) photon flux profile; (c) two-dimensional (2-D) profile of the middle frontal slice; (d) sagittal slice views of the 3-D photon flux profile; (e) 2-D profile of the middle sagittal slice; and (f) one-dimensional penetration profiles along the propagation directions of the frontal (open square), occipital (open circle), temporal (open triangle), parietal (filled circle), and north pole (filled square) source.

penetration depth-dependent enhancement results from the strengthened interference between sources as the examined intracranial site moves further away from the dominant source and approaches equidistance to all sources. Changing the light source emission profile from Gaussian to a narrowly shaped pencil beam produced virtually identical photon flux maps in both multi (crosses) and single (triangles) source simulations, likely due to the isotropic scattering approximation in the Monte Carlo model. That is, whether in form of a narrow pencil beam or a divergent Gaussian beam, the incident light is rapidly scattered out with equal probability in all directions, resulting in a similar expansion in beam width. Adjusting the anisotropic factor to higher values produced separation of the propagation profiles of the two beam types. All other simulation results presented here were obtained employing Gaussian beam parameters.

3.3 *Influence of Source Density*

Intuitively, higher-source density produces improved NIR penetration, but at the expense of higher-power consumption and increased heat generation at the semiconductor junctions. Optimal design of the radiation array calls for further understanding of the correlation between the intersource spacing and the penetration profile. Therefore, we repeated the simulations with a series of source numbers ranging from 13 to 277, the spatial arrangements and the density of which were determined by the above-mentioned rule (see Sec. 2). At each density, we studied the improvements in intracranial photon penetration in terms of enhanced flux and uniformity. Numbers of the light sources and the corresponding average solid angles are listed in Table 3. The consistently low (<10%) variations of the solid angle across the entire source density range, except at the minimal density of 13 sources, indicates a relatively even distribution of the sources.

The simulations yielded a progressively amplified gain of the photon flux as the source density increased (Fig. 5), and the progression slowed down at the source number of 181 and above. Increasing from 105 to 181 sources, the gain at the 60-mm penetration depth rose from 5× to 10×, yet a continued increase of the source number to 229 and 277 led to a decelerated further

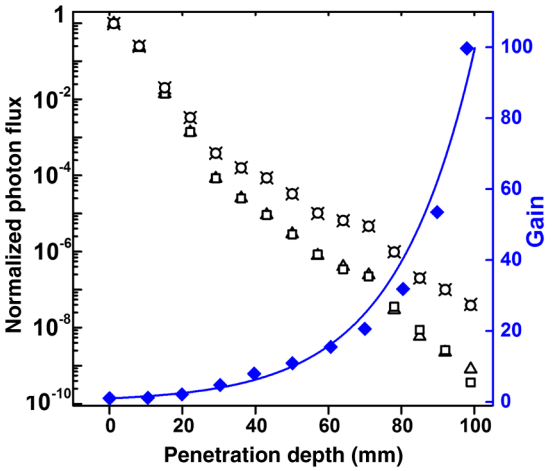

Fig. 4 Comparison of the penetration profiles of single versus multiple sources. Left axis (black): normalized photon flux along the propagation direction of the north pole source simulated with Gaussian (circles: multisource; squares: single source) vs. pencil beam (crosses: multisource; triangles: single source). Right axis (blue): ratio of the multi- versus single-source pencil-beam photon flux (i.e., the gain) shown by the black diamonds and fitted with an exponential function (solid line).

Table 3 Average solid angles and the SDs at different source densities.

Number of light sources	Weighted average of actual $\Delta\Omega$	SD of actual $\Delta\Omega$	SD over average
277	2.45×10^{-2}	1.23×10^{-3}	5.03%
229	2.99×10^{-2}	1.67×10^{-3}	5.57%
181	3.82×10^{-2}	2.61×10^{-3}	6.82%
105	6.80×10^{-2}	4.80×10^{-3}	7.06%
53	1.43×10^{-1}	1.17×10^{-2}	8.16%
13	7.02×10^{-1}	1.20×10^{-1}	17.16%

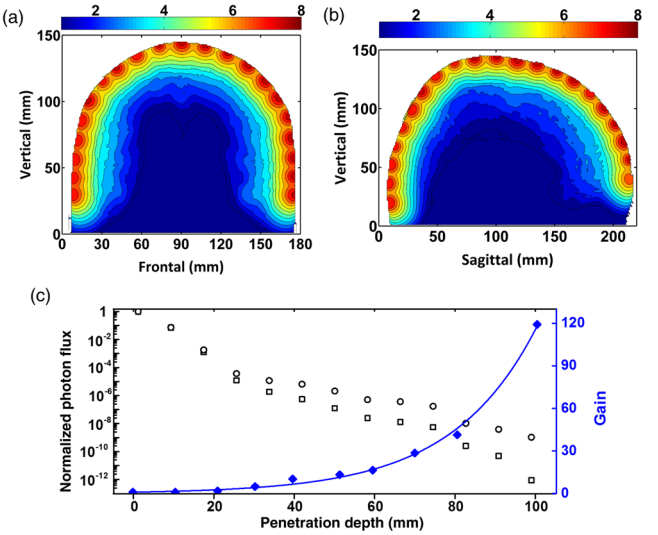

Fig. 6 Simulation of the transcranial penetration of 690 nm light: (a) 2-D representation of the photon flux color map of the middle frontal slice; (b) 2-D representation of the photon flux color map of the middle sagittal slice; and (c) left axis (black): photon flux decay profiles along the propagation direction of the north pole source, produced by multi (circles) versus single (squares). Right axis (blue): gain ratio of photon flux of multi- versus single-source at different penetration depths (solid diamonds), fitted with an exponential function (solid line).

enhancement in the photon flux. NIR radiation penetrating 60 mm deep into a human head is, in principle, sufficient to target the highly-convoluted cerebral cortex and a large portion of the white matter, which are often areas of interest for the therapeutic and diagnostic use of NIR. Therefore, photon flux enhancement up to a 60-mm depth is our main focus in determining the optimal number of emitters for the array.

In addition to the magnitude enhancement of the photon flux, improved uniformity of the radiation field was also obtained with increased light source density. This uniformity can be measured by the "relative SD" of the photon flux SD(photon flux)/mean(photon flux): the lower this value is, the more uniform the radiation is. It is observed that the relative SD decays exponentially with the number of light sources. Similar to the photon

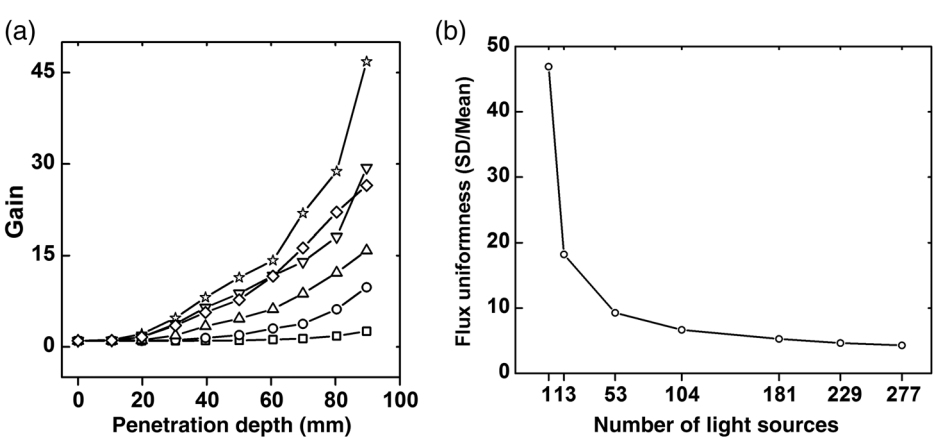

Fig. 5 Dependence of the photon penetration on the source density: (a) change of photon flux enhancement with penetration depth at various source densities. Penetration profiles obtained along the propagation direction of the north pole point at the source number, from high to low, of 277 (stars), 229 (diamonds), 181 (down triangles), 105 (up triangles), 53 (circles), and 13 (squares); and (b) uniformity of the photon flux (open circles) profile with the source number.

flux magnitude decay, the uniformity decay became less prominent at the source numbers of 181 and above. Taking the system complexity and the heat generation into account for the array design, the source density needs to be contained within a reasonable range. Our above analyses implicate an optimal density of 181 emitters, corresponding to a solid angle of ~0.04. This number was obtained under the assumption that each source is infinitesimally small, therefore, the real application may call for a reduced source density due to the larger radiation cross-section of individual sources.

3.4 *Influence of Reduced Wavelength*

To explore the multisource enhancement of the less penetrable red light, simulation of the transcranial propagation of the 690-nm light was also conducted. Table 2 lists the optical properties of tissues at this wavelength.[26] As presented in Fig. 6, switching from 850 to 690 nm light led to markedly accelerated intracranial photon flux attenuation along the propagation direction. For instance, a single 690-nm source at the north pole produced a ~1 to 2 orders of magnitude more exacerbated decay compared to a

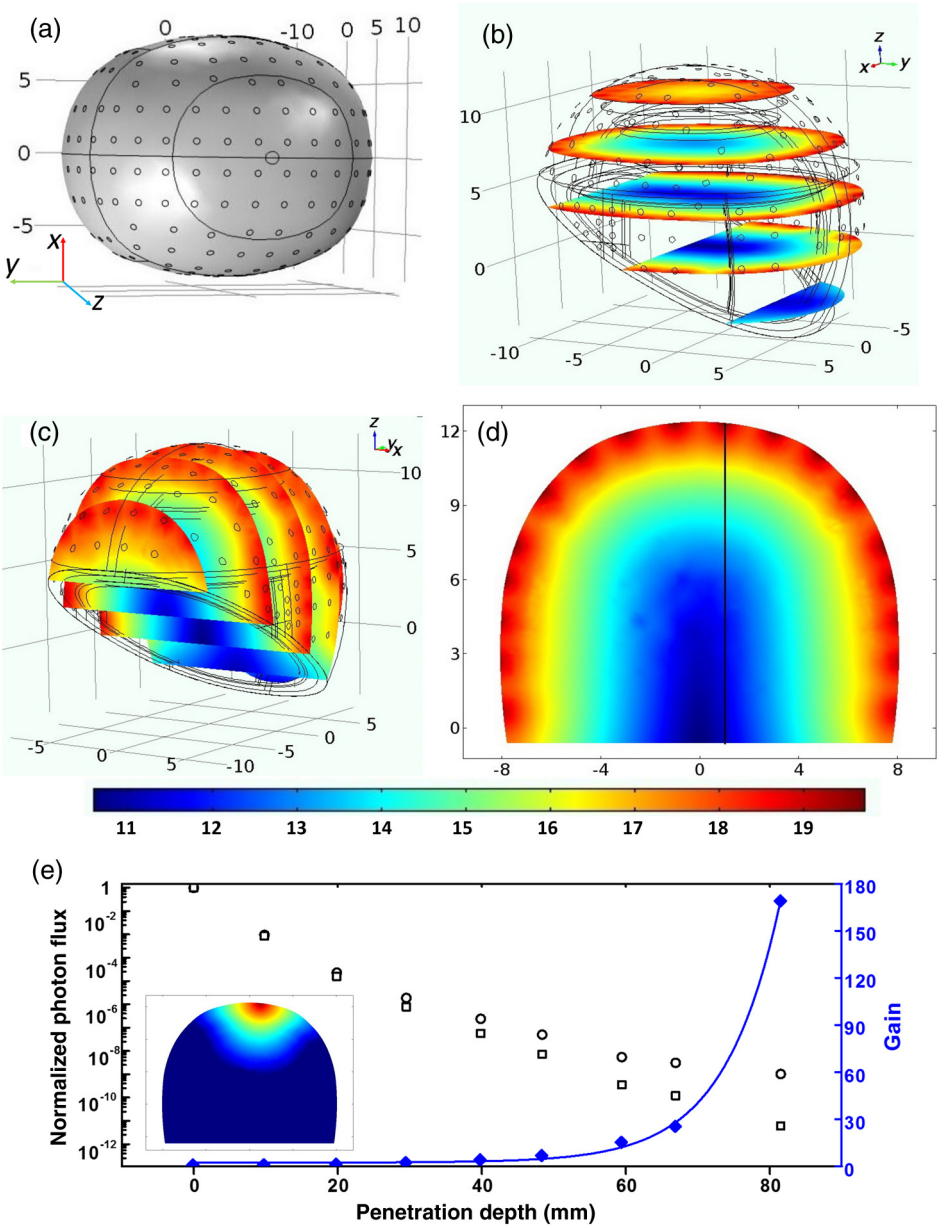

Fig. 7 850-nm near-infrared penetration profiles obtained with the diffusion equation finite element analysis: (a) spatial distribution of the sources on the scalp (small circles); (b) 3-D representation of the photon flux color map of the transverse slices; (c) 3-D representation of the photon flux color map of the frontal slices; (d) 2-D representation of the photon flux color map of the middle frontal slice. The black line shows the direction along which the photon flux was sampled and normalized in (e); (e) comparison of the photon flux decay profile from multi (open circles) versus single (open squares) source along the propagation direction labeled in (d). The ratios are shown by the solid diamonds and fitted with an exponential function. Inset: 2-D representation of the photon flux color map of the same slice in (d) but in the presence of only a single source.

single 850-nm source placed at the same location [compare squares in Figs. 4 and 6(c)]. On the other hand, cross enhancement between multiple sources was augmented for the shorter wavelength, arising from the increased scattering coefficients of the tissues. For example, the gain at a 40-mm depth increased from ~6× for 850 nm to ~10× for 690 nm light [compare black diamonds in Figs. 4 and 6(c)]. Similar to the results obtained with 850 nm, spatial changes of the photon flux enhancement with penetration depth is well characterized by a single exponential function, but with a faster increase ($\tau = 20.0 \pm 1.4$ mm^{-1}, $R^2 = 0.993$).

3.5 *Diffusion Equation Approach with Finite Element Method*

The diffusion approximation of the radiative transfer equation has been frequently used as an alternative approach to modeling photon migration in a turbid medium, though often deemed less accurate than the Monte Carlo simulation. Here, we developed a diffusion equation-based FEA model in parallel to the Monte Carlo method. The FEA model also contains scalp, skull, CSF, gray matter, and white matter layers, but with the fixed, instead of SPM segmented, thickness for more convenient meshing and less intensive computation. The tissue thicknesses were set based on our earlier measurements from the cadaveric samples as well as previously reported studies.[21,28] The diffusion approximation is only valid in scattering in the dominating medium and thus does not stand for weak scatterers such as CSF. Therefore, for this particular layer, the modified optical parameters ($\mu_a = 0.009$ mm^{-1}, $\mu_s' = 0.8$ mm^{-1}) that account for the scattering effect of arachnoid trabeculae was employed. The differences in the tissue segmentation and the optical properties between the FEA and the Monte Carlo modeling present difficulty in precise quantitative comparison, but do not hinder a qualitative verification.

Comparable to the Monte Carlo approach, FEA simulation with multiple sources yielded a rainbow-shaped quasiradially-symmetric photon flux map with small tangential variation [Figs. 7(a)–7(d)]. Application of multiple sources also produced enhancement in the photon flux that shows its dependence on the penetration depth, as illustrated in panel e. These qualitative resemblances between the results obtained from both models further verify the conceptual feasibility of using multiple sources for improved transcranial NIR radiation.

4 Conclusions

Transcranial NIR treatment of neurological diseases and brain trauma has gained momentum in the past decade. However, the low-NIR dose available to the brain, due to its severe scattering and absorption of the photons by the overlying tissues, largely limits its effectiveness in clinical use. Here, we propose to take advantage of the strong scattering effect of the cranial tissues by applying an evenly distributed multiemitter array on the scalp to enhance the cerebral photon density while maintaining each single emitter operating under the safe thermal and electrical limits. By employing the Monte Carlo method, we first simulated NIR penetration of each single light source, respectively, located in the frontal, occipital, temporal, parietal, and north pole regions of the human head model. The results obtained show comparable propagation profiles in all tested regions, largely consistent with our previous measurements from human cadaveric heads.[21] Moreover, we demonstrated that multiple sources produce markedly enhanced photon flux in the brain, as well as improved uniformity of the photon distribution, as revealed by the quasiradially-symmetric flux map and the reduced flux spatial variability. Not surprisingly, at a given wavelength, both the magnitude and the uniformity of the photon flux are governed by the source density. Our study suggests that 181 point sources evenly dispersed on the scalp, corresponding to an average solid angle of ~0.04, may be sufficient to generate a reasonably good photon flux map. More densely packed emitters tend to lead to only small further improvements in the upper-mid part of brain, which often coincides with the area of interest for the therapeutic NIR radiation. Our simulation did not take the blood flow into consideration, which, assuming relatively modest variations in the blood flow distribution in an adult head, may influence the attenuation rate of the photon flux, but is unlikely to result in a major impact on its spatial profile.

Previous studies[23] indicate that a single NIR LED introduces minimal radiation heat in biological tissues, but non-negligible conducted heat on the skin it is in direct contact with. The Monte Carlo simulation with multiple sources implies that at the maximum source density put forth here, photon flux enhancement will not necessarily cause alerting temperature elevations in the brain, since photon density superposition only substantialized beyond 2 cm from the scalp where the flux has already undergone a considerable decay. Additionally, blood circulation in the brain will enable faster heat dissipation. Nonetheless, thermal safety of the scalp-applied multiunit LED array merits further investigation, and attention needs to be directed to the conducted heat produced by the semiconductor junctions. Changing the radiation duration, pulse width, and duty cycle may reduce the heat generation.[23] In addition, optical fibers embedded in a helmet-like wearable can be used for light transmission, replacing the direct contact of the LED array with the scalp.

Coherent low-level NIR lasers have long been considered, by many, superior to the noncoherent sources in terms of tissue penetration efficiency. Yet the safety concern, due to its high-energy density, as well as the bulky equipment and the hefty cost make laser therapy difficult for home use. Our proposed approach using low-cost LED arrays to provide enhanced photon flux has the potential to be easily implemented for home care with minimal training. A recent study by Naeser et al.[13] suggests that upregulation of the whole-brain metabolic activity may play an important role in NIR-mediated neuroprotection against rotenone-induced retinotoxicity. Accordingly, multiple LED emitters may serve to promote the effectiveness of NIR treatment, especially in patients with multiloci lesions, by offering improved uniformity of the light field that exert therapeutic effects on larger surfaces of the brain.

The spatial configuration of the light source array may also find applications in optical diagnostics of the neurological diseases in the brain. Compared to the conventional single emitter–detector pair, back scattered light contributed by multiple sources may carry additional spatial and temporal information of the brain tissues in the area(s) of interest. With the proper computational algorithm, the signal received by the detector can be decoded and utilized for diagnostic analysis.

Acknowledgments

This work is supported by the W. M. Keck Foundation, the National Science Foundation (NSF) grant (Award No.: CBET-1404089), the Guangdong Innovative and Entrepreneurial

Research Team Program (No. 2013S046), and Shenzhen Peacock Plan, China.

References

1. M. A. Naeser and M. R. Hamblin, "Potential for transcranial laser or LED therapy to treat stroke, traumatic brain injury, and neurodegenerative disease," *Photomed. Laser Surg.* **29**(7), 443–446 (2011).
2. P. A. Lapchak, "Taking a light approach to treating acute ischemic stroke patients: transcranial near-infrared laser therapy translational science," *Ann. Med.* **42**(8), 576–586 (2010).
3. P. A. Lapchak and L. De Taboada, "Transcranial near infrared laser treatment (NILT) increases cortical adenosine-5'-triphosphate (ATP) content following embolic strokes in rabbits," *Brain Res.* **1306**, 100–115 (2010).
4. Y. Lampl et al., "Infrared laser therapy for ischemic stroke: a new treatment strategy: results of the neurothera effectiveness and safety trial-1 (NEST-1)," *Stroke* **38**(6), 1843–1849 (2007).
5. J. A. Zivin et al., "Effectiveness and safety of transcranial laser therapy for acute ischemic stroke," *Stroke* **40**(4), 1359–1364 (2009).
6. W. Hacke et al., "Transcranial laser therapy in acute stroke treatment: results of neurothera effectiveness and safety trial 3, a phase III clinical end point device trial," *Stroke* **45**(11), 3187–3193 (2014).
7. P. A. Lapchak et al., "Transcranial near-infrared light therapy improves motor function following embolic strokes in rabbits: an extended therapeutic window study using continuous and pulse frequency delivery modes," *Neuroscience* **148**(4), 907–914 (2007).
8. A. Oron et al., "Low-level laser therapy applied transcranially to mice following traumatic brain injury significantly reduces long-term neurological deficits," *J. Neurotrauma* **24**(4), 651–656 (2007).
9. M. S. Moreira et al., "Effect of phototherapy with low intensity laser on local and systemic immunomodulation following focal brain damage in rat," *J. Photochem. Photobiol. B* **97**(3), 145–151 (2009).
10. W. Xuan et al., "Transcranial low-level laser therapy enhances learning, memory, and neuroprogenitor cells after traumatic brain injury in mice," *J. Biomed. Opt.* **19**(10), 108003 (2014).
11. W. Xuan et al., "Low-level laser therapy for traumatic brain injury in mice increases brain derived neurotrophic factor (BDNF) and synaptogenesis," *J. Biophotonics* **8**(6), 502–511 (2014).
12. Y. Y. Huang et al., "Transcranial low level laser (light) therapy for traumatic brain injury," *J. Biophotonics* **5**(11–12), 827–837 (2012).
13. M. A. Naeser et al., "Improved cognitive function after transcranial, light-emitting diode treatments in chronic, traumatic brain injury: two case reports," *Photomed. Laser Surg.* **29**(5), 351–358 (2011).
14. F. Schiffer et al., "Psychological benefits 2 and 4 weeks after a single treatment with near infrared light to the forehead: a pilot study of 10 patients with major depression and anxiety," *Behav. Brain Funct.* **5**, 46 (2009).
15. L. De Taboada et al., "Transcranial laser therapy attenuates amyloid-beta peptide neuropathology in amyloid-beta protein precursor transgenic mice," *J. Alzheimers Dis.* **23**(3), 521–535 (2011).
16. H. Moges et al., "Light therapy and supplementary riboflavin in the SOD1 transgenic mouse model of familial amyotrophic lateral sclerosis (FALS)," *Lasers Surg. Med.* **41**(1), 52–59 (2009).
17. J. R. Jagdeo et al., "Transcranial red and near infrared light transmission in a cadaveric model," *PLoS One* **7**(10), e47460 (2012).
18. J. T. Eells et al., "Therapeutic photobiomodulation for methanol-induced retinal toxicity," *Proc. Natl. Acad. Sci.* **100**(6), 3439–3444 (2003).
19. M. T. Wong-Riley et al., "Photobiomodulation directly benefits primary neurons functionally inactivated by toxins: role of cytochrome c oxidase," *J. Biol. Chem.* **280**(6), 4761–4771 (2005).
20. L. Zhang et al., "Low-power laser irradiation inhibiting Abeta25-35-induced PC12 cell apoptosis via PKC activation," *Cell. Physiol. Biochem.* **22**(1–4), 215–222 (2008).
21. L. Yue et al., "Simulation and measurement of transcranial near infrared light penetration," *Proc. SPIE* **9321**, 93210S (2015).
22. Y. Ito et al., "Assessment of heating effects in skin during continuous wave near infrared spectroscopy," *J. Biomed. Opt.* **5**(4), 383–390 (2000).
23. A. Bozkurt and B. Onaral, "Safety assessment of near infrared light emitting diodes for diffuse optical measurements," *Biomed. Eng. Online* **3**(1), 9 (2004).
24. C. J. Holmes et al., "Enhancement of MR images using registration for signal averaging," *J. Comput. Assisted Tomogr.* **22**(2), 324–333 (1998).
25. Q. Fang and D. A. Boas, "Monte Carlo simulation of photon migration in 3D turbid media accelerated by graphics processing units," *Opt. Express* **17**(22), 20178–20180 (2009).
26. J. W. Barker, A. Panigrahy, and T. J. Huppert, "Accuracy of oxygen saturation and total hemoglobin estimates in the neonatal brain using the semi-infinite slab model for FD-NIRS data analysis," *Biomed. Opt. Express* **5**(12), 4300–4312 (2014).
27. S. L. Jacques, "Optical properties of biological tissues: a review," *Phys. Med. Biol.* **58**(11), R37–R61 (2013).
28. E. Okada and D. T. Delpy, "Near-infrared light propagation in an adult head model. I. Modeling of low-level scattering in the cerebrospinal fluid layer," *Appl. Opt.* **42**(16), 2906–2914 (2003).
29. D. Boas et al., "Three dimensional Monte Carlo code for photon migration through complex heterogeneous media including the adult human head," *Opt. Express* **10**(3), 159–170 (2002).
30. H. Dehghani et al., "The effects of internal refractive index variation in near-infrared optical tomography: a finite element modelling approach," *Phys. Med. Biol.* **48**(16), 2713–2727 (2003).
31. M. Schweiger et al., "The finite element method for the propagation of light in scattering media: boundary and source conditions," *Med. Phys.* **22**(11 Pt 1), 1779–1792 (1995).
32. E. Okada et al., "Theoretical and experimental investigation of near-infrared light propagation in a model of the adult head," *Appl. Opt.* **36**(1), 21–31 (1997).

Lan Yue received her bachelor's degree in electronic engineering from the University of Science and Technology of China in 2006 and subsequently obtained her PhD in bioengineering from the University of Illinois at Chicago in 2012. Currently, she is a postdoctoral research associate at the University of Southern California. Her research focuses on biophotonic and bioelectronic therapeutics for a variety of neural disorders ranging from retinal degeneration to brain trauma.

Mark S. Humayun is a university professor with joint appointments in ophthalmology and cell and neurobiology at the Keck School of Medicine, and in Biomedical Engineering at the Viterbi School of Engineering, University of Southern California. He holds the Cornelius J. Pings Chair in biomedical sciences. He is an expert in biomedical technology and the retina, director of the University of Southern California (USC) Institute for Biomedical Therapeutics and the Sensory Sciences Institute, and codirector of the USC Eye Institute.